IET Radar, Sonar & Navigation

WILEY

The Institution of Engineering and Technology

ORIGINAL RESEARCH OPEN ACCESS

Grating Lobe Suppression of Non-Periodic Geometric Formations Based on Modified Particle Swarm Optimization

Lin Qiu[1,2] | Huijie Liu[1] | Juan Chen[3] | Hao Huang[4] | Andrew W. H. Ip[5] | Kai Leung Yung[5]

[1]Innovation Academy for Microsatellites of Chinese Academy of Sciences, Shanghai, China | [2]University of Chinese Academy of Sciences, Beijing, China | [3]Shanghai Spacecom Satellite Technology, Ltd. Shanghai, China | [4]Hubei Key Lab of Ferro & Piezoelectric Materials and Devices, Faculty of Physics and Electronic Science, Hubei University, Wuhan, China | [5]Department of Industrial and Systems Engineering, The Hong Kong Polytechnic University, Kowloon, Hong Kong

Correspondence: Lin Qiu (qiulin39@126.com)

Received: 17 February 2025 | **Revised:** 3 April 2025 | **Accepted:** 23 May 2025

Handling Editor: Hugh Griffiths

Funding: This work is supported in part by the Youth Innovation Promotion Association of the Chinese Academy of Sciences under (Grant No. 2022296), in part by the Hubei Province International Scientific Research Cooperation Project under (Grant No. 2023EHA035) in part by the Research Centre for Deep Space Explorations of the Hong Kong Polytechnic University (Grant No. K-45-35-ZPEV).

Keywords: aerospace engineering | antenna radiation patterns | particle swarm optimization | space-based radar | synthetic aperture radar

ABSTRACT

For the issue of configuration difficulty in maintaining linear formations based on the same orbital plane for distributed space-based coherent aperture radar (DSCAR), it is necessary to modify the linear formation model into an arc formation model. This article derives the steering vector and joint pattern expressions for DSCAR based on uniform arc formation, and designs a segmented inertial factor (IF) particle swarm optimization (PSO) to seek the optimal solution for non-uniform spacing and random yaw angle in non-periodic geometric distribution. Simulation analysis shows that the combination of non-uniform spacing and random yaw angle in non-periodic geometric formations can achieve lower peak side lobe level (PSLL) compared to single non-uniform spacing and single random yaw angle but with wider beamwidth spread. Additionally, the segmented IF PSO proposed in this article balances convergence more quickly in the early stage of the search process and improves convergence speed to approach the optimal value (OV) in later stage. Compared with other IF PSO, it has better convergence speed and accuracy.

1 | Introduction

Space-based radar systems have the working characteristics of all-day, all-weather and global coverage, and occupy a special and important position in modern warfare. By employing space-based means, long-range wide-area reconnaissance, identification, detection, tracking and high-precision guidance of moving targets can be achieved. Based on the formation, group and constellation of space-based radar, ultra-long range defence operations can be realised in key directions and areas, breaking through the interception limitations of ground terrain, earth curvature and other factors on ground defence weapon systems, thereby significantly enhancing defensive combat capabilities [1–4].

Distributed space-based coherent aperture radar (DSCAR) is a new-type space-based radar system which is composed of multiple satellite radar units (RU) that can be quickly launched and deployed. Through coherent signal fusion and superposition, it

can be equivalently synthesised into an ultra-large virtual aperture array antenna, achieving spatial coherent processing while improving angular resolution and detection accuracy. However, optimizing the design of each RU to minimise the side lobe level of the array, thereby improving the DSCAR detection capability, is one of the key contents in distributed radar research [5–9] which is also the core of our study.

If the RUs in DSCAR are uniformly geometrically distributed according to a certain baseline, the joint pattern will inevitably exhibit grating lobe with levels almost identical to the main lobe. Here, we can draw inspiration from the idea of reducing grating lobe techniques in non-periodic phased array antennas. The phased array is divided into multiple subarrays, and each subarray redistributed grating lobe energy to the sidelobe region through methods such as rotation, sparsity and displacement to reduce grating lobe peak level and achieve grating lobe suppression [10–18]. The authors from reference [10] achieved side lobe suppression by randomly rotating each antenna element in the phased array, but the spacing between antenna elements remained at half wavelength and was uniformly distributed. The authors from references [11, 12] explored the design of planar phased arrays with subarrays arranged in an irregular domino shape, optimizing position and orientation using genetic algorithms to achieve lower side lobe levels. The authors from reference [13] proposed a modular asymmetric convex subarray which constructed the array through rotation and translation, filled the aperture without overlapping or gaps and achieved lower grating lobe. The authors from reference [14] achieved grating lobe suppression by rotating phased array antennas which is suitable for low-frequency sparse aperture array antenna systems of square kilometre array radio telescopes with symmetrical spiral structures. However, the rotation angle only provided typical values based on approximate function values without providing an optimal solution. The authors from reference [15] used virtual antenna filling to suppress the grating lobe and perform angle estimation which is suitable for sparse arrays. The authors from reference [16] proposed an optimization algorithm based on position gradient and sigmoid function for non-uniform arrays which can achieve lower side lobe. The authors from reference [17] theoretically studied the effect of non-uniform linear distributed array spacing and element number on the elimination of the grating lobe, ensuring signal favourable propagation in MIMO systems under different incidence conditions but only achieving partial grating lobe elimination. The authors from reference [18] proposed an adaptive gradient search algorithm for displacement subarray optimization which can effectively suppress the grating lobe.

However, the aforementioned studies have two main limitations. Firstly, existing methods only consider either rotation angle or non-uniform spacing as a single parameter for grating/side lobe suppression, rather than a joint optimization approach. Secondly, the parameter optimization techniques used in prior work do not achieve the best possible grating/side lobe suppression. To address the first gap, this article proposes a joint optimization method combining non-uniform spacing and rotation angle, comparing its performance against single-parameter approaches. For the second gap, we designed a segmented inertia factor PSO and compared its performance with other inertia factor PSOs, aiming to provide an advanced improved PSO algorithm and a new reference solution for grating lobe suppression in DSCAR. The particle swarm optimization (PSO) algorithm, as a prominent swarm intelligence method, is widely favoured in beamforming design [19–21]. At the same time, in order to meet diverse application scenarios, it is necessary to seek further improvements in the convergence speed, convergence accuracy, stability and other aspects of PSO. Among the parameters of PSO, the inertia factor (IF), is the most important parameter which plays a crucial role in improving the performance of PSO. The authors from reference [22] considered the PSO performance with two constant IFs. The authors from reference [23] proposed a linear decreasing IF for evaluating the performance of PSO. The authors from reference [24] proposed a parabolic form decreasing IF adjustment strategy which degrades to a linear decreasing IF when the index is 1. The authors from reference [25] designed an IF adjustment that decrease exponentially. The authors from reference [26] offered the chaotic random IF based on the traversal and randomness characteristics of chaotic mapping. The authors from reference [27] proposed an adaptive IF for PSO stability. The authors from reference [28] summarised 18 inertia factor control strategies, derived the conditions required for these strategies to exhibit convergent behaviour and evaluated these strategies based on benchmark problem sets. Therefore, various IFs have certain limitations in solving application scenario problems. Their performance cannot comprehensively guide diverse scenarios and still need to be continuously and thoroughly tested and verified. This article focuses on the design of low side lobe beamforming for DSCAR, aiming to reduce the time required for antenna pattern simulation. We expect to achieve improved convergence speed within a limited number of iterations and ideal convergence accuracy by modified IF.

Section 2 proposes a DSCAR model based on uniform arc formation (UAF) and derives the joint pattern formula. Section 3 modified the joint pattern formula based on non-periodic geometric formations. To reduce the grating lobe in the joint pattern of DSCAR, a segmented IF PSO is constructed to optimize the design of three non-periodic geometric formations, including non-uniform spacing distribution, random angle yaw and their joint distribution, in Section 4. Simulation analysis provided peak side lobe level (PSLL) and beamwidth results for the three non-periodic geometric formations, and verified the performance of the segmented inertia factor PSO in Section 5. Finally, Section 6 concludes this article.

2 | Joint Pattern Model of UAF-DSCAR

Assuming that each RU antenna is co-located for transmitting antenna and receiving antenna, and the plane wave signal $\boldsymbol{S}$ is incident on each RU of DSCAR at an angle θ, the received signal $\boldsymbol{Y}$ of DSCAR can be expressed as follows:

$$\boldsymbol{Y} = \boldsymbol{a}(\theta)\boldsymbol{S}, \tag{1}$$

where $\boldsymbol{a}(\theta)$ is the steering vector of DSCAR and can be given by the following equation:

$$\boldsymbol{a}(\theta) = \boldsymbol{a}_{\mathrm{ISL}}(\theta) \otimes \boldsymbol{a}_{\mathrm{RU}}(\theta), \tag{2}$$

here, $\boldsymbol{a}_{\mathrm{ISL}}(\theta)$ is the steering vector between RUs based on the inter-satellite link, $\boldsymbol{a}_{\mathrm{RU}}(\theta)$ is the incident signal steering vector of single RU and $\otimes$ is the Kronecker product operation.

Because all RUs have the same orbital height, DSCAR is no longer a strictly linear formation but an arc formation as Figure 1 shows.

In general, RUs on the same orbital plane exhibit an equal phase distribution that the spacing between adjacent RUs is D. In this configuration, DSCAR functions as a UAF. If the baseline spacing of DSCAR satisfies both the short baseline condition and far-field condition, each RU can be regarded as the translation of RU_1 along the arc. According to the geometric relationship of phase difference, $\boldsymbol{a}_{\mathrm{ISL}}(\theta)$ can be denoted by the following equation:

$$\boldsymbol{a}_{\mathrm{ISL}}(\theta)=\begin{bmatrix} 1 \\ e^{j2\xi(R+H)\sin\frac{\phi_1^{\mathrm{UAF}}}{2}\sin\left(\theta+\frac{\phi_1^{\mathrm{UAF}}}{2}\right)} \\ \vdots \\ e^{j2\xi(R+H)\sin\frac{\phi_{K-1}^{\mathrm{UAF}}}{2}\sin\left(\theta+\frac{\phi_{K-1}^{\mathrm{UAF}}}{2}\right)} \end{bmatrix}, \tag{3}$$

where R represents the average radius of the earth and H represents the orbital height of RUs. ϕ_k^{UAF} represents the phase difference between $\mathrm{RU_k}$ and $\mathrm{RU_1}$ in UAF and is derived as follows:

$$\phi_k^{\mathrm{UAF}}=\frac{kD}{R+H}. \tag{4}$$

If a uniform linear array antenna is arranged in RU, the steering vector $\boldsymbol{a}_{\mathrm{RU}}(\theta)$ can be expressed as follows:

$$\boldsymbol{a}_{\mathrm{RU}}(\theta)=\begin{bmatrix} 1 \\ e^{j\xi d\sin\theta} \\ \vdots \\ e^{j\xi(M-1)d\sin\theta} \end{bmatrix}, \tag{5}$$

In Equation (5), $\xi=2\pi/\lambda$, scalar d and M represent the element spacing and element number of RU, respectively.

The essence of antenna pattern $F(\theta)$ is the weighted vector accumulation of steering vectors from different spatial angles at the desired beam angle and is defined by the following equation:

$$F(\theta)=\boldsymbol{\omega}^H(\theta)\boldsymbol{a}(\theta), \tag{6}$$

$\boldsymbol{\omega}$ is the weight coefficient of the array filter. Let $\boldsymbol{\omega}_{\mathrm{ISL}}=\boldsymbol{a}_{\mathrm{ISL}}(\theta_{\mathrm{dir}})$ and $\boldsymbol{\omega}_{\mathrm{RU}}=\boldsymbol{a}_{\mathrm{RU}}(\theta_{\mathrm{dir}})$ where θ_{dir} is the peak angular value of θ. In addition, we define $F_{\mathrm{ISL}}(\theta)$ as the inter-RU array pattern and $F_{\mathrm{RU}}(\theta)$ as the intra-RU array pattern. By changing the filter weight coefficient $\boldsymbol{\omega}$, the joint pattern based on UAF can be obtained by the following equation:

$$F_{\mathrm{DSCAR-UAF}}(\theta)=\left|\sum_{k=0}^{K-1} I_k e^{-j2\xi(R+H)\sin\frac{\phi_k^{\mathrm{UAF}}}{2}\left[\sin\left(\theta+\frac{\phi_k^{\mathrm{UAF}}}{2}\right)-\sin\left(\theta_{\mathrm{dir}}+\frac{\phi_k^{\mathrm{UAF}}}{2}\right)\right]}\right| \cdot \left|\sum_{m=0}^{M-1} I_m e^{-j\xi md(\sin\theta-\sin\theta_{\mathrm{dir}})}\right| \tag{7}$$

I_k and I_m represent the excitation of the kth RU and the excitation of the mth antenna unit in the linear array of RU,

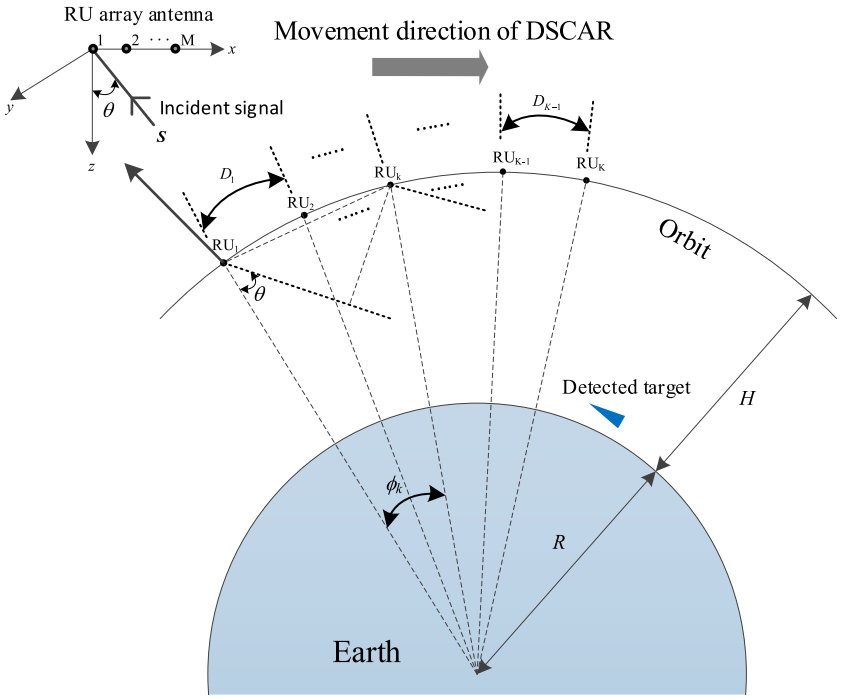

FIGURE 1 | DSCAR model with UAF.

respectively. For simplification, both of them are taken as 1 here.

3 | Non-Periodic Spatial Geometric Distribution Method

Because of the fact that UAF belongs to a uniformly spaced distributed array, and the spacing between RUs is much larger than half wavelength, this inevitably results in a large number of grating lobes, leading to an increase in side lobe level. By effectively disrupting the periodic energy accumulation of a uniform distributed array through the non-periodic spatial geometric distribution of RU, the purpose of suppressing grating lobe can be achieved. The spatial geometric distribution methods mainly include RU non-uniform spacing and RU angle rotation that we call it angle yaw in this article.

For our proposed UAF model, the reference uniform angle difference $\Delta\phi_k^{\mathrm{UAF}} = D/(R+H)$ can be disrupted and theoretically achieved low side effects by using non-uniform spacing formation. If AF is a non-uniform arc formation (NUAF), then the phase difference $\Delta\phi_k^{\mathrm{UAF}}$ correction in Equation (4) is modified as follows:

$$\phi_k^{\mathrm{NUAF}} = \sum_{k=1}^{K-1} \frac{D_k}{R+H}. \tag{8}$$

Therefore, Equation (3) is given as follows:

$$\boldsymbol{a}_{\mathrm{ISL}}(\theta) = \begin{bmatrix} 1 \\ e^{j2\xi(R+H)\sin\frac{\phi_1^{\mathrm{NUAF}}}{2}\sin\left(\theta+\frac{\phi_1^{\mathrm{NUAF}}}{2}\right)} \\ \vdots \\ e^{j2\xi(R+H)\sin\frac{\phi_{K-1}^{\mathrm{NUAF}}}{2}\sin\left(\theta+\frac{\phi_{K-1}^{\mathrm{NUAF}}}{2}\right)} \end{bmatrix}. \tag{9}$$

The joint pattern of NUAF is derived as follows:

$$\begin{aligned} F_{\mathrm{DSCAR-NUAF}}(\theta) &= F_{\mathrm{ISL}}(\theta)F_{\mathrm{RU}}(\theta) \\ &= \left[\boldsymbol{\omega}_{\mathrm{ISL}}^H(\theta_{\mathrm{dir}})\boldsymbol{a}_{\mathrm{ISL}}(\theta)\right]\left[\boldsymbol{\omega}_{\mathrm{RU}}^H(\theta_{\mathrm{dir}})\boldsymbol{a}_{\mathrm{ISL}}(\theta)\right] \\ &= \left|\sum_{k=0}^{K-1} e^{-j2\xi(R+H)\sin\frac{\phi_k^{\mathrm{NUAF}}}{2}\left[\sin\left(\theta+\frac{\phi_k^{\mathrm{NUAF}}}{2}\right)-\sin\left(\theta_{\mathrm{dir}}+\frac{\phi_k^{\mathrm{NUAF}}}{2}\right)\right]}\right| \\ &\quad \cdot \left|\sum_{m=0}^{M-1} e^{-j\xi md(\sin\theta-\sin\theta_{\mathrm{dir}})}\right| \end{aligned} \tag{10}$$

Similar to the rotation method of phased array antenna subarray, the grating lobe suppression can also be achieved to a certain extent by yaw angle of each RU. There are two methods to achieve RU angle yaw. One is to rotate the RU antenna installation but the structural forms of each RU is different. This is not conducive to the unified design of RU structures and each RU must be strictly ordered. The other is to unify the design of each RU with only the yaw angle of attitude that this article adopts.

The yaw angles of all RU are denoted by $[\varphi_0, \varphi_2, \cdots, \varphi_{K-1}]$, respectively, and $\varphi_0 = 0$; the steering vector between RUs is modified as follows:

$$\boldsymbol{a}_{\mathrm{ISL}}(\theta) = \begin{bmatrix} 1 \\ e^{j2\xi(R+H)\sin\frac{\phi_1^{\mathrm{UAF}}}{2}\sin\left(\theta+\frac{\phi_1^{\mathrm{UAF}}}{2}\right)\cos\varphi_1} \\ \vdots \\ e^{j2\xi(R+H)\sin\frac{\phi_{K-1}^{\mathrm{NUAF}}}{2}\sin\left(\theta+\frac{\phi_{K-1}^{\mathrm{NUAF}}}{2}\right)\cos\varphi_{K-1}} \end{bmatrix}. \tag{11}$$

Constrained by the angle control capability of the satellite platform's solar array drive assembly and the range of angles for inter-satellite communication payload, we limit the maximum yaw angle range of each RU to $[-45°, 45°]$. Combining Equations (8) and (11), the joint pattern $F_{\mathrm{DSCAR-NUAF}}(\theta)$ based on NUAF is modified as follows:

$$\begin{aligned} F_{\mathrm{DSCAR-NUAF}}(\theta) &= \left|\sum_{k=0}^{K-1} e^{-j2\xi(R+H)\sin\phi_k^{\mathrm{NUAF}}\cos\varphi_k\left[\sin\left(\theta+\phi_k^{\mathrm{NUAF}}\right)-\sin\left(\theta_{\mathrm{dir}}+\phi_k^{\mathrm{NUAF}}\right)\right]}\right| \\ &\quad \cdot \left|\sum_{m=0}^{M-1} e^{-j\xi md(\sin\theta-\sin\theta_{\mathrm{dir}})}\right| \end{aligned} \tag{12}$$

Similarly, the joint pattern $F_{\mathrm{DSCAR-UAF}}(\theta)$ based on UAF can be obtained by the following equation:

$$\begin{aligned} F_{\mathrm{DSCAR-UAF}}(\theta) &= \left|\sum_{k=0}^{K-1} e^{-j2\xi(R+H)\sin\phi_k^{\mathrm{UAF}}\cos\varphi_k\left[\sin\left(\theta+\phi_k^{\mathrm{UAF}}\right)-\sin\left(\theta_{\mathrm{dir}}+\phi_k^{\mathrm{UAF}}\right)\right]}\right| \\ &\quad \cdot \left|\sum_{m=0}^{M-1} e^{-j\xi md(\sin\theta-\sin\theta_{\mathrm{dir}})}\right| \end{aligned} \tag{13}$$

In order to effectively suppress the peak side lobe caused by grating lobe, we take the peak side lobe level as the fitness function for optimization variables, and PSLL is defined as follows:

$$\mathrm{PSLL} = \max_{\theta_s}\left\{\left|\frac{F_{\mathrm{DSCAR}}(\theta,\varphi)}{\max[F_{\mathrm{DSCAR}}(\theta,\varphi)]}\right|\right\}, \tag{14}$$

where θ_s is the side lobe range of the joint pattern, and fitness function of optimization model is given by the following equation:

$$\begin{aligned} \min(\mathrm{PSLL}) = &\begin{cases} P(\varphi_1, \varphi_2, \cdots, \varphi_K), \text{UAF with angle yaw} \\ P(D_1, D_2, \cdots, D_{K-1}), \text{NUAF without angle yaw} \\ P(\varphi_1, \varphi_2, \cdots, \varphi_K, D_1, D_2, \cdots, D_{K-1}), \text{NUAF with angle yaw} \end{cases} \\ &\text{s.t.} \\ &\varphi_1 = 0, |\varphi_i| \le 45°, 1 \le i \le K \\ &D_1 = 0, \lambda \le D_j \le 5000\lambda, 1 \le j \le K-1 \end{aligned} \tag{15}$$

4 | Modified PSO Based on Segemented if

From Equation (15), it can be seen that the angles that UAF needs to optimize are the K-dimensional variable, whereas

NUAF requires both spacing and angles to be 2(K-1)-dimensional variables. This places higher demands on the convergence speed and accuracy of the selected optimization algorithm. The PSO is inspired by the collective behaviour of bird flocks, utilising information sharing and collaboration among individuals to find the optimal solution. The core principle formula is as follows:

$$\begin{cases} v_i = \omega v_i + c_1 \text{rand}()(\text{pbest}_i - x_i) + c_2 \text{rand}()(\text{gbest} - x_i) \\ x_i = x_i + v_i \end{cases}, \quad (16)$$

x_i and v_i represent the position and velocity of ith particle, respectively. The historical optimal positions of ith particle and particle swarm are denoted as pbest_i and gbest, respectively. ω is the IF. c_1 and c_2 are learning factors. rand() generates the random number in the interval $[0, 1]$.

In Equation (16), the objects that can be optimized are IF and learning factors. A gradually decaying IF helps to explore a larger range in the early stages and gradually converge in the later stages. Dynamic or adaptive learning factors help balance the exploration and development abilities of individual particles. This article focuses on optimizing the IF. We expect that IF should be relatively large and the particles should be dispersed in the early stage so as to conduct a global search to avoid premature convergence and falling into local optima. It is necessary to have a smaller value of IF and more concentrated particles for local search to achieve more accurate solutions in the later stage. Therefore, we propose a segmented inertia factor as follows:

$$\omega(t) = \begin{cases} \omega_{\max} - \sin\left(\frac{\pi t}{T}\right)\omega_{\min}, t \le \frac{T}{2} \\ (\omega_{\max} - \omega_{\min})\left(1 - \frac{t}{T}\right)^2 + \omega_{\min}, t > \frac{T}{2} \end{cases}. \quad (17)$$

In the first half of the stage, we design a sinusoidal increasing method to disperse particles and conduct global search to improve convergence speed. In the latter half of the stage, we switch to a parabolic descent method to concentrate particles, conduct local search and accurately approximate the optimal solution.

5 | Simulation Results

We select the following parameter values for simulation as shown in Table 1.

TABLE 1 | Main simulation parameters.

Parameter	Value
K	6
θ_{dir}	0°
M	20
R	6378137m
H	500000m

5.1 | Performance of Segmented IF PSO

Before simulating Equation (15), we first evaluate the performance of the segmented IF PSO based on Equation (17). Here, we use 23 sets of test functions commonly used in computational intelligence competition for validation [29] where F1–F7 are unimodal benchmark functions, F8–F13 are multimodal benchmark functions and F14–F23 are composite benchmark test functions. The expressions of test functions are shown in Appendix: Table A1. The iteration count is set to 50 times.

In addition, we selected some representative IF PSO and compared their performance with the segmented IF PSO proposed in this article including constant IF PSO [22], linear IF PSO [23], parabolic IF PSO [24], exponential IF PSO [25] and chaotic random IF PSO [26].

In terms of convergence accuracy, Table 2 presents the results of conducting 200 independent tests on 23 sets of test functions for six types of IF PSO including the segmented IF proposed in this article. The optimal value (OV) of each IF PSO is chosen from 200 independent tests. For the same test function, the red font represents the unique OV, whereas the green font indicates that at least two types of PSO can achieve the same value.

It can be seen that various IF PSO with iterations of 50 times cannot converge precisely to the theoretical OV for the unimodal benchmark functions from F1 to F7 and the multimodal benchmark functions from F8 to F13. Except for function F7 which can converge relatively well and approach the theoretical OV, the others seriously deviate from theoretical OV. However, we can still observe that the segmented IF PSO and constant IF PSO perform equally well for benchmark functions F1–F13. Both of them basically cover the lowest values achievable by benchmark functions F1-together, performing slightly better than other IF PSO. This also confirms the conclusion that the constant IF PSO remains a relatively effective PSO for solving any optimization problem in reference [28]. However, the segmented IF PSO in this article also demonstrates excellent convergence accuracy on multiple benchmark functions.

For the composite benchmark test functions from F14 to F23, except for function F15 which has a similar degree of closeness to the theoretical OV, the test OV of all other functions can achieve consistency with the theoretical OV within 50 iterations for six types of IF PSO.

Beside the OV, Table 2 also provides statistical results such as mean value (MV), standard deviation (SD), mean rank (MR) and median. These statistical results can better characterise the robustness and stability of algorithm convergence. For MV, segmented IF PSO get a best ranking in functions F1, F5, F6, F8, F10–F15, F22 and F23, and share a pretty ranking in functions F16, F17 and F19 with other IF PSO. For SD, segmented IF PSO ranks high in functions F6, F10, F11, F13–F15 and F19, and tie for first place in F20 with constant IF PSO. For MR, segmented IF PSO has best performance in functions F1, F5, F6 and F10–F14. For the median, segmented IF PSO shines in functions F1, F5, F6, F8, F10–F14 and F16–F23. The results indicate that segmented IF PSO achieves better performance on functions F1, F5, F6, F8 and F10–F23.

TABLE 2 | Statistical results of the 23 test functions.

Test function	Theoretical OV	Test OV	Constant IF PSO	Linear IF PSO	Parabolic IF PSO	Exponential IF PSO	Chaotic random IF PSO	Segmented IF PSO	Rank of segmented IF PSO
F1	0	OV	**247.89**	1936.66	2440.40	1816.96	2452.85	916.91	2
		MS	4519.59	4142.97	5276.39	4066.66	7411.31	**3787.69**	**1**
		SD	1663.15	1377.53	1531.91	**1271.63**	2320.40	1321.37	2
		MR	720.02	448.41	680.18	434.71	946.85	**372.85**	**1**
		Median	5524.59	3971.65	5292.16	4013.62	7290.57	**3600.72**	**1**
F2	0	OV	**10.01**	20.25	20.80	18.15	25.03	16.62	2
		MS	**37.13**	37.31	42.03	38.43	42.12	37.75	3
		SD	11.69	11.28	11.41	9.85	**9.46**	12.28	6
		MR	**514.57**	534.87	693.08	592.34	724.13	544.03	3
		Median	**34.12**	35.18	39.78	37.47	40.70	35.27	3
F3	0	OV	3642.30	5327.84	5539.47	4975.00	4286.98	**3455.00**	**1**
		MS	**12,040.85**	13,626.10	14,814.64	13,258.39	16,432.87	13,418.70	3
		SD	4705.49	4847.19	5735.74	**4270.57**	6265.27	4587.19	2
		MR	**461.10**	588.65	655.25	575.72	745.93	576.37	3
		Median	**10,987.44**	12,868.26	13,856.94	12,824.00	15,457.51	12,788.60	2
F4	0	OV	15.41	19.72	20.68	20.09	22.87	**14.49**	**1**
		MS	31.69	**28.92**	31.84	30.30	35.44	29.63	2
		SD	4.65	**4.42**	5.27	4.81	5.62	4.82	4
		MR	636.26	**447.18**	644.18	542.44	847.26	485.69	2
		Median	31.53	**28.71**	32.04	30.22	35.14	29.01	2
F5	0	OV	**1.80E+04**	1.76E+05	3.99E+05	2.08E+05	8.05E+05	2.80E+04	2
		MS	2.22E+06	1.25E+06	2.12E+06	1.39E+06	4.44E+06	**1.19E+06**	**1**
		SD	1.32E+06	**7.94E+05**	1.38E+06	9.26E+05	2.59E+06	8.11E+05	2
		MR	6.90E+02	4.19E+02	6.56E+02	4.68E+02	9.77E+02	**3.92E+02**	**1**
		Median	2.05E+06	1.03E+06	1.81E+06	1.17E+06	3.77E+06	**9.55E+05**	**1**
F6	0	OV	**501**	1947	2679	1249	3256	946	2
		MS	4612.09	3904.05	5298.96	4115.40	7206.92	**3725.74**	**1**
		SD	1544.40	1333.19	1655.47	1422.54	2170.19	**1262.13**	**1**
		MR	745.71	410.10	680.13	450.47	939.56	**376.54**	**1**
		Median	5626.50	3829.50	5238.00	3922.50	7067.50	**3613.50**	**1**
F7	0	OV	0.79	1.52	1.89	0.66	1.00	**0.4**	**1**
		MS	7.58	7.13	9.22	6.50	**5.52**	6.33	2
		SD	**3.69**	4.82	5.69	4.99	3.95	4.88	4
		MR	692.13	608.29	752.64	548.54	**474.24**	527.17	2
		Median	7.13	5.47	7.76	5.16	**4.54**	4.89	2
F8	−12569.5	OV	**−7716.27**	−6850.44	−5866.68	−6910.39	−5297.36	−6764.85	4
		MS	−5453.26	−5594.07	−5061.43	−5486.37	−4174.57	**−5603.48**	**1**
		SD	825.75	757.17	712.76	718.99	**677.82**	771.99	5
		MR	520.31	**457.31**	673.76	502.33	989.09	460.21	2
		Median	−5397.18	−5577.85	−5094.35	−5515.34	−4186.15	**−5641.19**	**1**
F9	0	OV	65.26	92.34	129.11	106.96	121.88	**60.54**	**1**
		MS	**127.46**	158.82	179.14	157.33	171.20	171.51	5

(Continues)

TABLE 2 | (Continued)

Test function	Theoretical OV	Test OV	Constant IF PSO	Linear IF PSO	Parabolic IF PSO	Exponential IF PSO	Chaotic random IF PSO	Segmented IF PSO	Rank of segmented IF PSO
		SD	**21.79**	27.37	27.47	27.33	26.43	29.31	6
		MR	**233.92**	569.41	805.82	562.81	719.83	711.22	4
		Median	**127.75**	154.94	179.36	156.78	170.18	168.72	4
F10	0	OV	7.84	9.53	10.56	9.54	11.57	**7.77**	**1**
		MS	13.49	12.20	13.13	12.21	13.93	**11.82**	**1**
		SD	1.15	1.22	1.16	1.36	**1.14**	1.25	**1**
		MR	773.82	445.75	683.01	462.11	876.02	**362.31**	**1**
		Median	13.57	12.27	13.14	12.36	13.91	**11.86**	**1**
F11	0	OV	**7**	16.53	16.23	11.16	32.74	7.4	2
		MS	52.58	35.86	49.65	37.82	65.29	**33.79**	**1**
		SD	14.88	12.13	13.84	12.55	19.89	**10.40**	**1**
		MR	761.86	404.12	710.87	445.70	927.87	**352.59**	**1**
		Median	50.91	34.28	48.72	36.11	63.11	**32.48**	**1**
F12	0	OV	12.78	**12.45**	16.91	24.03	135.58	16.21	3
		MS	1.15E+05	4.59E+04	1.81E+05	3.21E+04	7.72E+05	**2.49E+04**	**1**
		SD	1.95E+05	9.91E+04	3.30E+05	**6.79E+04**	1.10E+06	7.20E+04	2
		MR	651.37	459.59	720.03	440.97	935.94	**395.12**	**1**
		Median	4.02E+04	4.84E+03	5.92E+04	4.59E+03	3.17E+05	**1.98E+03**	**1**
F13	0	OV	**75.33**	56,746.18	71,066.99	13,413.99	184,487.81	2293.49	2
		MS	2.31E+06	1.30E+06	2.50E+06	1.19E+06	7.17E+06	**9.39E+05**	**1**
		SD	2.42E+06	1.55E+06	2.40E+06	1.20E+06	8.09E+06	**1.10E+06**	**1**
		MR	650.50	461.90	680.63	462.58	960.29	**387.11**	**1**
		Median	1.57E+06	8.11E+05	1.70E+06	7.96E+05	5.30E+06	**5.54E+05**	**1**
F14	1	OV	**1**	**1**	**1**	**1**	**1**	**1**	**1**
		MS	7.35	5.16	5.86	5.26	6.84	**4.76**	**1**
		SD	4.80	4.02	4.40	4.26	4.56	**3.81**	**1**
		MR	706.64	545.88	602.16	534.07	678.32	**529.47**	**1**
		Median	6.90	3.48	3.97	3.97	6.90	**3.38**	**1**
F15	3.075E-04	OV	3.90E-04	3.96E-04	**3.19E-04**	4.42E-04	4.06E-04	3.22E-04	2
		MS	5.33E-03	4.45E-03	5.61E-03	4.45E-03	9.52E-03	**3.84E-03**	**1**
		SD	1.05E-02	8.13E-03	8.78E-03	9.16E-03	1.42E-02	**6.83E-03**	**1**
		MR	**5.25E+02**	5.48E+02	6.62E+02	5.81E+02	7.55E+02	5.32E+02	2
		Median	**1.36E-03**	1.66E-03	2.35E-03	1.73E-03	3.75E-03	1.55E-03	2
F16	−1.0316	OV	**−1.0316**	**−1.0316**	**−1.0316**	**−1.0316**	**−1.0316**	**−1.0316**	**1**
		MS	−1.0275	**−1.0316**	**−1.0316**	**−1.0316**	**−1.0316**	**−1.0316**	**1**
		SD	**5.77E-02**	3.98E-11	1.25E-05	1.29E-11	2.01E-06	1.56E-07	3
		MR	934.70	689.12	328.80	688.56	**53.05**	789.32	5
		Median	**−1.0316**	**−1.0316**	**−1.0316**	**−1.0316**	**−1.0316**	**−1.0316**	**1**
F17	0.398	OV	**0.398**	**0.398**	**0.398**	**0.398**	**0.398**	**0.398**	**1**
		MS	**0.398**	**0.398**	**0.398**	**0.398**	0.412	**0.398**	**1**
		SD	1.28E-11	7.75E-11	3.67E-08	5.80E-05	**9.50E-02**	1.81E-08	3
		MR	905.62	608.26	272.18	628.19	**248.23**	740.88	5
		Median	**0.398**	**0.398**	**0.398**	**0.398**	0.412	**0.398**	**1**

(Continues)

TABLE 2 | (Continued)

Test function	Theoretical OV	Test OV	Constant IF PSO	Linear IF PSO	Parabolic IF PSO	Exponential IF PSO	Chaotic random IF PSO	Segmented IF PSO	Rank of segmented IF PSO
F18	3	OV	**3**	**3**	**3**	**3**	**3**	**3**	**1**
		MS	4.62	3.41	4.62	**3.00**	5.49	3.41	3
		SD	10.36	5.73	11.37	**0.00**	9.09	5.73	2
		MR	948.18	653.55	350.56	671.59	258.19	715.87	5
		Median	**3**	**3**	**3**	**3**	**3**	**3**	**1**
F19	−3.86	OV	**−3.86**	**−3.86**	**−3.86**	**−3.86**	**−3.86**	**−3.86**	**1**
		MS	−3.85	**−3.86**	−3.85	−3.85	−3.82	**−3.86**	**1**
		SD	0.02	0.02	0.03	0.03	0.04	**0.01**	**1**
		MR	516.50	440.31	714.56	**438.14**	953.66	539.77	4
		Median	**−3.86**	**−3.86**	**−3.86**	**−3.86**	−3.84	**−3.86**	**1**
F20	−3.32	OV	**−3.32**	**−3.32**	**−3.32**	**−3.32**	**−3.32**	**−3.32**	**1**
		MS	**−3.24**	−3.22	−3.21	−3.22	−2.84	−3.23	2
		SD	**0.15**	0.16	0.17	0.16	0.37	**0.15**	**1**
		MR	**447.52**	504.26	621.22	500.10	998.07	531.85	4
		Median	−3.31	**−3.32**	−3.25	**−3.32**	−2.95	**−3.32**	**1**
F21	−10	OV	**−10.15**	**−10.15**	**−10.15**	**−10.15**	**−10.15**	**−10.15**	**1**
		MS	−5.51	−4.97	**−4.89**	−4.91	−5.15	−5.26	2
		SD	3.28	**2.84**	2.87	2.96	3.23	2.95	3
		MR	**467.01**	565.52	658.96	558.23	719.90	633.40	4
		Median	−5.06	−5.08	−2.68	−2.68	−2.68	**−5.10**	**1**
F22	−10	OV	**−10.40**	**−10.40**	**−10.40**	**−10.40**	**−10.40**	**−10.40**	**1**
		MS	−5.53	−5.39	−5.53	−5.55	−5.42	**−5.87**	**1**
		SD	3.46	3.26	3.37	3.42	**3.24**	3.47	6
		MR	**528.92**	586.73	626.58	548.22	695.93	616.63	4
		Median	−3.72	−3.72	−3.72	−3.72	−3.72	**−5.09**	**1**
F23	−10	OV	**−10.54**	**−10.54**	**−10.54**	**−10.54**	**−10.54**	**−10.54**	**1**
		MS	−6.00	−5.57	−5.10	−5.11	−5.17	**−6.07**	**1**
		SD	3.67	3.57	**3.27**	3.42	3.41	3.71	6
		MR	**486.10**	576.24	648.44	581.56	705.39	605.29	4
		Median	**−3.84**	−2.87	−2.87	−2.87	−2.87	**−3.84**	**1**

In terms of convergence speed, we depict the corresponding convergence process for each value in Table 2 as shown in Figure 2. Compared to other IF PSO, the segmented IF PSO proposed in this article has a much faster convergence speed. Among them, the initial stages of functions F2 and F17 have basically converged to the optimal test value. Functions F4, F7, F9, F10, F18 and F20 not only converge quickly but also converge to the test OV closest to the theoretical OV. Although functions F11 and F12 did not achieve the optimal test value they have the fastest convergence speed. The convergence speed of functions F21, F22 and F23 is second only to the chaotic random IF PSO. Among the remaining functions, the convergence speed of the segmented IF PSO still ranks in the upper–middle range.

Furthermore, the segmented IF PSO can quickly converge and smoothly approach the test OV and will converge precisely to the test OV after 25 iterations for all functions except for functions F8, F9 and F10 that are still in the process of convergence and descent after 25 iterations.

It is worth pointing out that the test functions F10 and F20 can be regarded as simplified version of the fitness function expression mentioned in Equation (14) of this article, which are same in the form of exponential summation, and the power expression of the exponent are also similar in the form of summation. Moreover, the segmented IF PSO in this article can obtain the OV consistent with theory in the test function F20. This indicates that the segmented IF PSO in this article is suitable for optimizing Equation (14). Furthermore, the minimum PSLL obtained from NUAF side lobe simulation, UAF random angle yaw side lobe simulation or NUAF random angle yaw side lobe simulation is theoretically close to the optimal PSLL value.

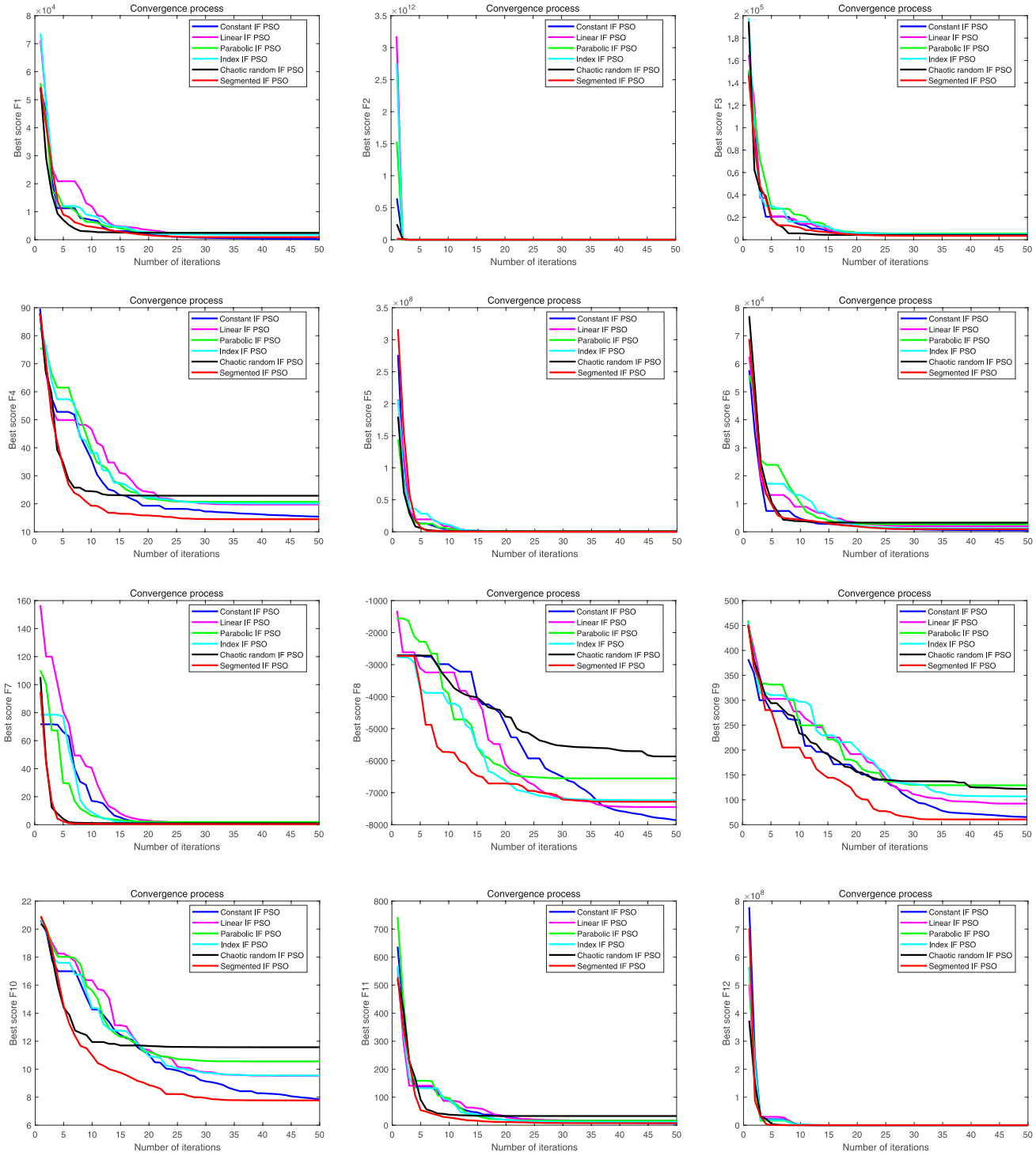

FIGURE 2 | 23 sets of test function convergence curves.

5.2 | Side Lobe Simulation Results of NUAF

Here, we first consider selecting some typical spacing D samples for UAF spacing, and then constrain the spacing D_j range of NUAF in Equation (15) within $[0.5D, 1.5D]$ for optimization. Taking the reference spacing $D = 3000\lambda$ as an example, the corresponding range of NUAF spacing D_j is $[1500\lambda, 4500\lambda]$ as shown in Table 3. To ensure the convergence accuracy of PSLL minimum, we set the number of single optimization iterations to 500. After 20 independent iteration simulation tests, the minimum of PSLL is −4.977 dB, the maximum is −4.051 dB and the average is −4.441 dB. When the UAF spacing decreases to 300λ, the corresponding PSLL suppression effect of NUAF is equivalent to 3000λ. When the UAF spacing decreases to 30λ and 3λ, the average of PSLL based on NUAF can reach −10.186 dB and −30.235 dB, respectively. The difference between the maximum and minimum of PSLL obtained from multiple optimizations is only about 1 dB at each spacing.

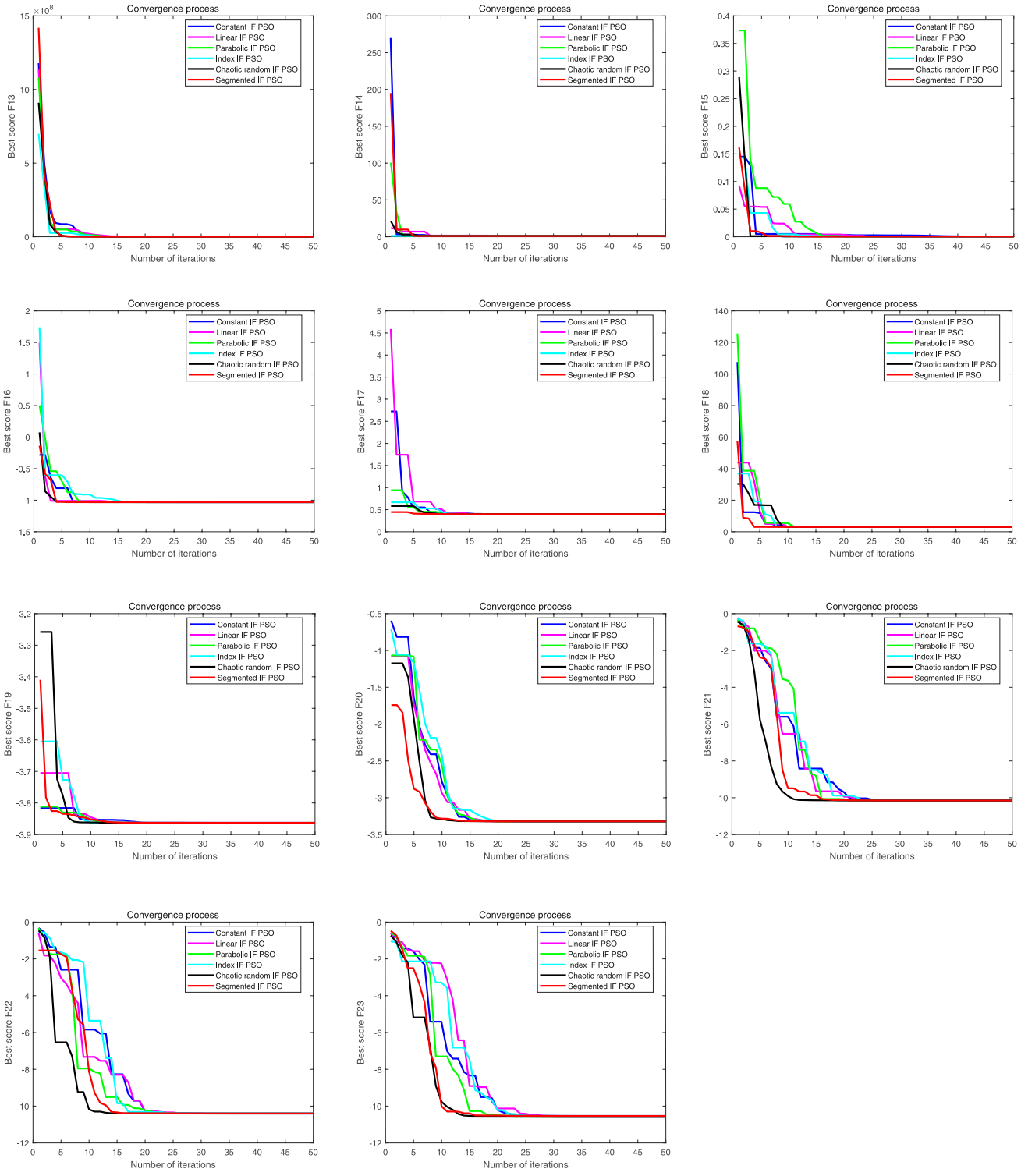

FIGURE 2 | (Continued)

Figure 3 shows the optimal PSLL suppression results for several different spacing ranges of NUAF based on 20 independent iteration tests. In addition, the figures also show the variation of the 3 dB beamwidth of NUAF compared to UAF. Here, the joint pattern is limited by the number of simulation points and cannot be infinitely large. Only the approximate 3 dB beamwidth of the two directional patterns is marked on the joint pattern. Taking the reference spacing $D = 3000\lambda$ as an example, the beamwidth with a 3.118 dB decrease in peak of UAF is 0.0029°, whereas the beamwidth with a 2.889 dB decrease in peak of NUAF reaches 0.0031°. Hence, the 3 dB beamwidth of NUAF is widened by more than 1.07 times compared to UAF. Similarly, when the reference spacing is $D = 300\lambda$, $D = 30\lambda$ and $D = 3\lambda$, the 3 dB beamwidth of NUAF is widened by more

TABLE 3 | Side lobe simulation results of NUAF.

Reference spacing D of UAF	Spacing range $[0.5D, 1.5D]$ of NUAF	NUAF PSLL (dB)		
		Minimum	**Maximum**	**Average**
3000λ	$[1500\lambda, 4500\lambda]$	−4.977	−4.051	−4.441
300λ	$[150\lambda, 450\lambda]$	−5.102	−4.102	−4.527
30λ	$[15\lambda, 45\lambda]$	−10.812	−9.710	−10.186
3λ	$[1.5\lambda, 4.5\lambda]$	−30.486	−29.782	−30.235

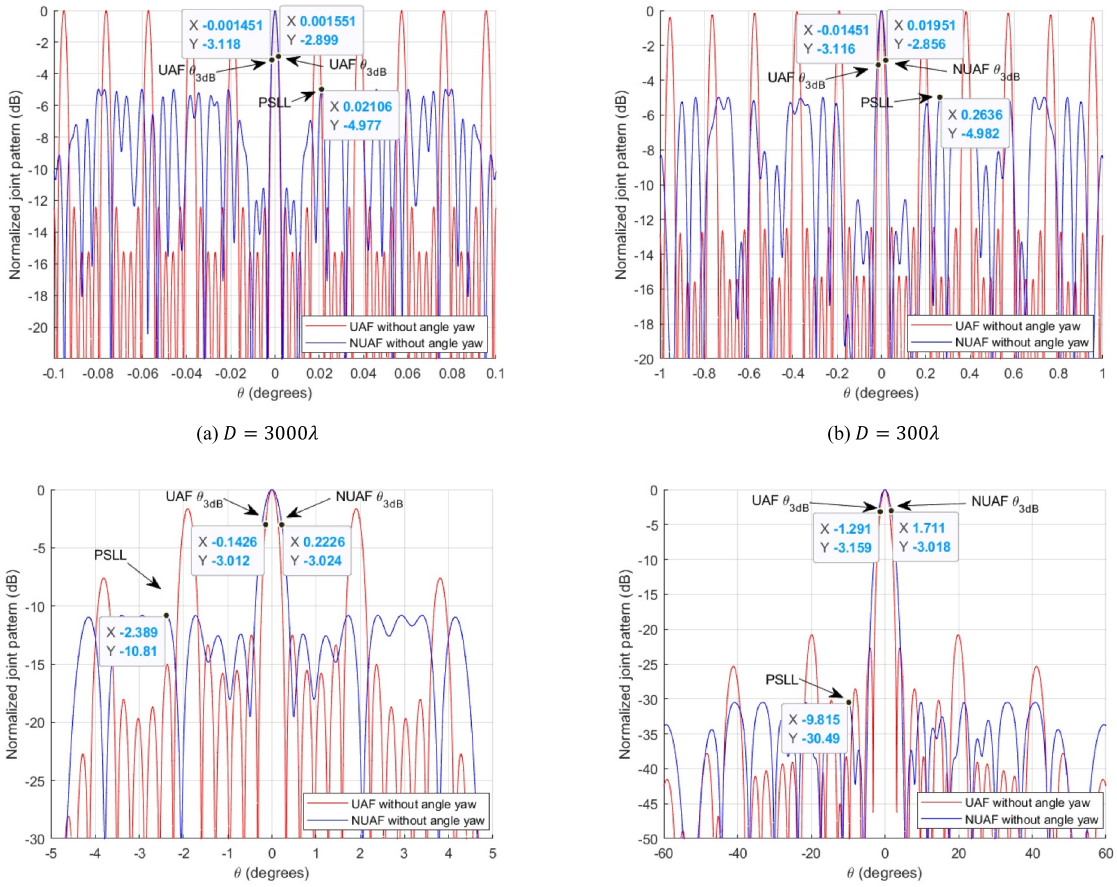

(a) $D = 3000\lambda$ (b) $D = 300\lambda$

(c) $D = 30\lambda$ (d) $D = 3\lambda$

FIGURE 3 | The NUAF joint pattern of PSLL minimum at different reference spacing.

than 1.34 times, 1.56 times and 1.33 times, respectively. Further, Table 4 gives the non-uniform spacing values corresponding to the four joint pattern in Figure 3.

In the process of 20 independent iterative tests, the joint pattern of NUAF may exhibit two or more identical PSLL results for a certain reference spacing D but the corresponding $[D_1, D_2, \cdots, D_{K-1}]$ is not the unique solution. Table 4 only displays one set of the solution. It can be seen that the OV of D_k tends towards the lower limit of interval $[0.5D, 1.5D]$, leading to an equivalent synthesised aperture of NUAF being smaller than that of UAF. According to beamforming theory, the 3 dB beamwidth is inversely proportional to the spacing and number of antenna elements, so the equivalent synthesised aperture of NUAF becomes smaller after optimization which in turn affects the broadening of the joint pattern to a certain extent.

Here, we still use the reference spacing $D = 3000\lambda$ as an example. After 20 independent iteration tests, Figure 4a–c show the convergence processes of NUAF after 50 iterations, 100 iterations and 500 iterations, respectively with the corresponding PSLL minimum being −4.561, −4.963 and −4.977 dB. We can observe that the first half of the convergence process has a higher convergence rate, whereas the second half converges slightly to the current optimal solution. As the number of iterations increases, the convergence accuracy improves such that the PSLL minimum approaches the OV at around 100 iterations. Accordingly, we provide the PSLL suppression results for different IF

TABLE 4 | Comparison of equivalent synthetic aperture between UAF and NUAF.

UAF		NUAF					
Reference spacing D	**Equivalent synthetic aperture**	D_1	D_2	D_3	D_4	D_5	**Equivalent synthetic aperture**
3000λ	15000λ	3237.7λ	1629.4λ	2726.6λ	3733.3λ	2189.2λ	$13{,}516.2\lambda$
300λ	1500λ	217.8λ	389.9λ	270.3λ	167.5λ	328.2λ	1373.7λ
30λ	150λ	25.3λ	19.1λ	15.0λ	15.0λ	37.8λ	112.2λ
3λ	15λ	3.0λ	1.5λ	1.5λ	2.0λ	2.1λ	10.1λ

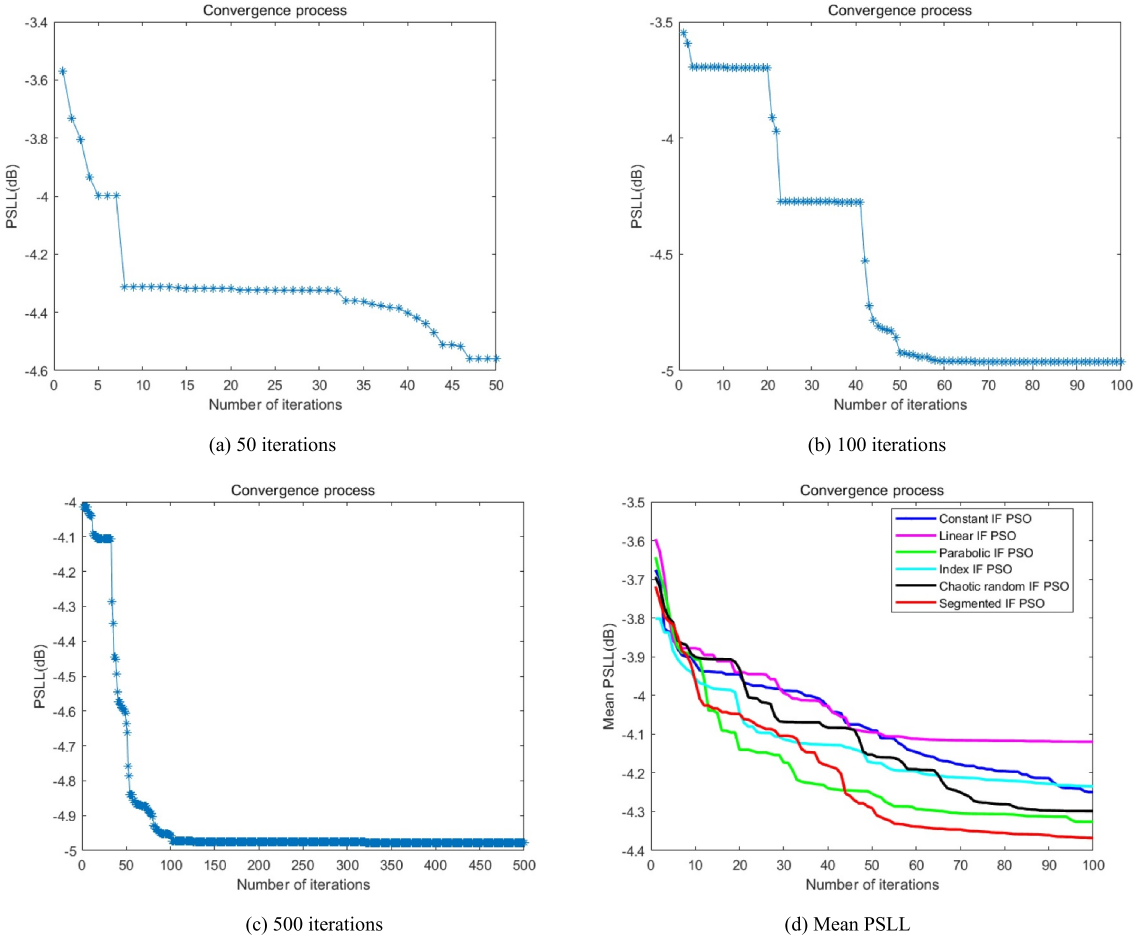

(a) 50 iterations (b) 100 iterations

(c) 500 iterations (d) Mean PSLL

FIGURE 4 | PSLL suppression results.

PSO after 100 iterations. Segmented IF PSO still exhibits faster convergence and higher convergence accuracy in Figure 4d.

5.3 | Side Lobe Simulation Results of UAF Random Angle yaw

If the random angle yaw is adopted to obtain low side lobe for UAF, we also consider selecting typical spacing samples of 3000λ, 300λ, 30λ and 3λ, and optimize the yaw angle φ_i constrained within $[-45°, 45°]$ according to Equation (15). As shown in Table 5, we set the number of single optimization iterations to 500 and conduct 20 independent iteration simulation tests. When the UAF spacing is 3000λ and 300λ the optimal results of PSLL suppression are only -2.899 and -2.953 dB, respectively. This indicates that the suppression effect is not ideal when the number of RUs is 6 and the number of RU antenna elements is 20. At this time, it is necessary to increase the number of RUs or RU antenna elements to obtain a lower PSLL. When the UAF spacing is reduced to 30λ, the average suppression result of PSLL is -3.583 dB which can meet the requirement of less than -3 dB. When the spacing is further reduced to 3λ, the lowest suppression result of PSLL can reach -27.14dB, the highest suppression result is -24.632dB and the average value of 20 times is -26.317dB. When the UAF spacing is small, a lower PSLL suppression effect can still be achieved through random angle yaw. However, the overall optimal suppression effect based on UAF random angle yaw is not as good as NUAF under the same conditions. The 3dB

TABLE 5 | Side lobe simulation results of the UAF random angle yaw.

Reference spacing D of UAF	PSLL of UAF random angle yaw (dB)		
	Minimum	**Maximum**	**Average**
3000λ	−2.899	−2.670	−2.796
300λ	−2.953	−2.714	−2.821
30λ	−3.5833	−3.5831	−3.58325
3λ	−27.140	−24.632	−26.317

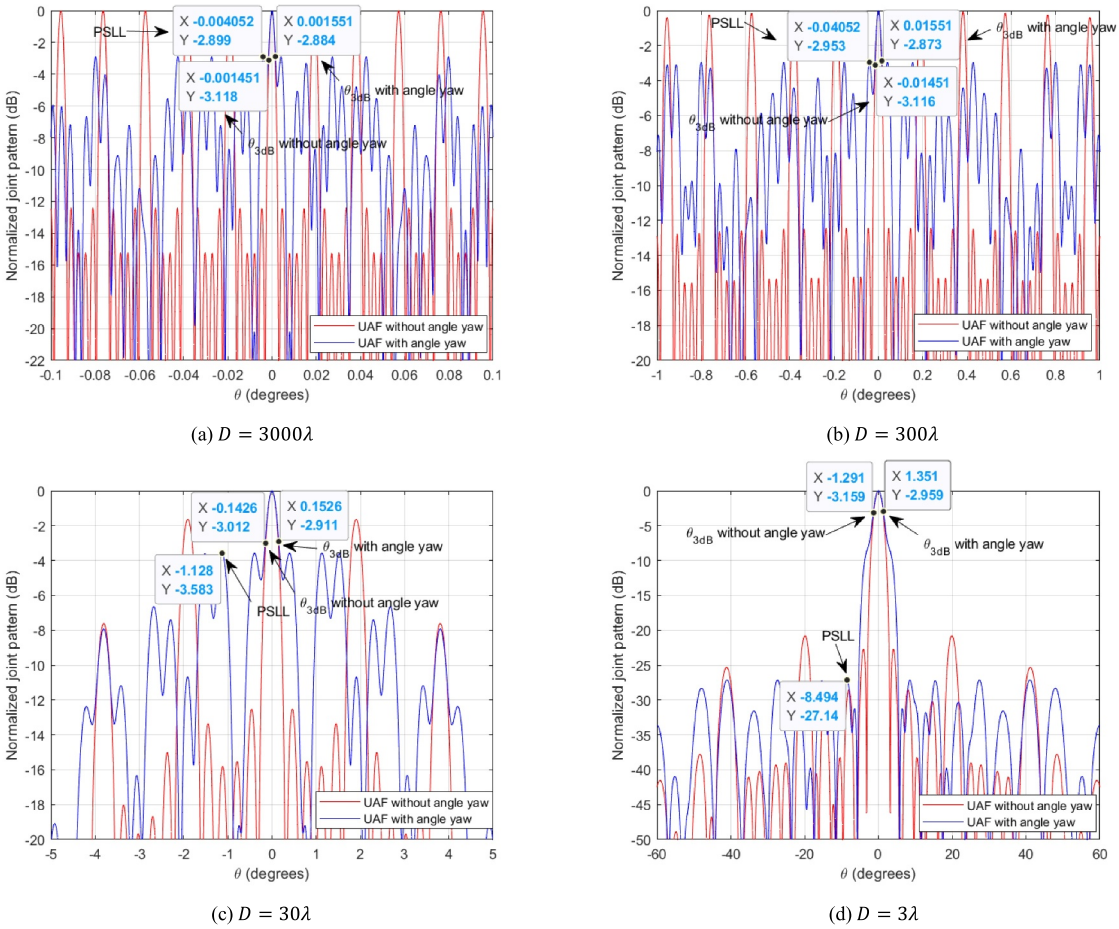

(a) $D = 3000\lambda$ (b) $D = 300\lambda$

(c) $D = 30\lambda$ (d) $D = 3\lambda$

FIGURE 5 | UAF with the random angle yaw joint pattern of PSLL minimum at different reference spacing.

beamwidth of the joint pattern after the random angle yaw is approximately 1.07 times, 1.07 times, 1.07 times and 1.05 times wider than that of UAF at four spacings from large to small, respectively. Compared with the 3 dB beamwidth of NUAF shown in Figure 3, the beamwidth widening is not significant in Figure 5.

Here, we still take the reference spacing $D = 3000\lambda$ as an example. After 20 independent iteration tests, Figure 6a–c show the convergence process of NUAF after 50 iterations, 100 iterations and 500 iterations, respectively. The corresponding minimum PSLL are −2.896, −2.8984 and −2.8985 dB. It can be seen that the convergence process of the UAF random angle yaw is similar to that of NUAF. However, the PSLL minimum approaches the OV around 50 iterations which converges faster than NUAF. Figure 6d shows that the convergence speed and accuracy of segmented IF PSO and constant IF PSO are consistent and outstanding.

5.4 | Side Lobe Simulation Results of the NUAF Random Angle yaw

In this section, we analyse the joint optimization effect of the non-uniform spacing distribution and random angle yaw. We still choose the same simulation parameters. If the UAF reference spacing is D, the corresponding NUAF random yaw angle φ_i range is constrained within $[-45°, 45°]$ and the spacing D_j range is constrained within $[0.5D, 1.5D]$. The number of single optimization iterations and independent iteration simulation tests are set to 500 and 20, respectively. The simulation test

results are shown in Table 6. Compared with Table 3, the minimum of PSLL for the four reference spacings are further reduced by 0.274, 1.082, 5.01 and 0.551 dB, respectively, whereas the average values are reduced by 0.438, 0.656, 4.174 and 0.586 dB, respectively. It can be seen that the joint optimization of the non-uniform spacing distribution and random angle yaw can achieve lower PSLL on the basis of single optimization of non-uniform spacing distribution, and the optimization effect is more significant at $D = 30\lambda$.

Figure 7 shows the NUAF joint pattern of PSLL minimum at different reference spacing based on random angle. The 3 dB beamwidth of the joint pattern is widened by about 1.34, 1.76, 2.61 and 1.37 times compared to UAF, respectively, which is wider than the NUAF beamwidth. Especially with $D = 30\lambda$, although PSLL achieves lower values, the corresponding beamwidth broadening is greater.

We also take the reference spacing $D = 3000\lambda$ as an example. After 20 independent iteration tests, Figure 8a–c show the convergence process of iteration 50, 100 and 500 times, respectively. The corresponding minimum PSLL values are −5.064, −5.234 and −5.251 dB. The convergence process of the NUAF random angle yaw is also similar to that of NUAF. After more than 100 iterations, the minimum value of PSLL basically approaches the OV which converges faster than NUAF. Moreover, there is still room for a decrease in the PSLL minimum at around 500 iterations. Figure 8d presents that segmented IF

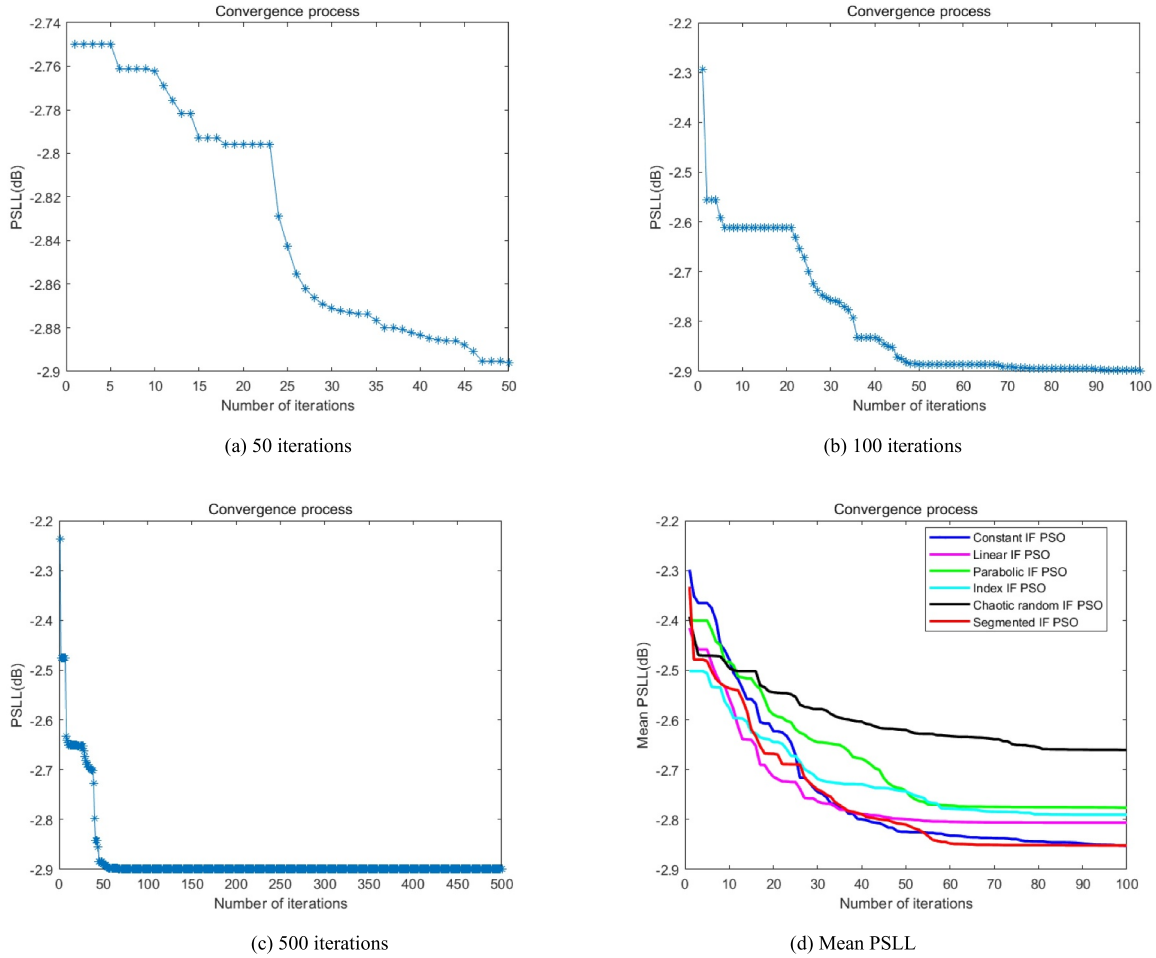

(a) 50 iterations

(b) 100 iterations

(c) 500 iterations

(d) Mean PSLL

FIGURE 6 | PSLL suppression results.

TABLE 6 | Side lobe simulation results of the NUAF random angle yaw.

	PSLL of NUAF random angle yaw (dB)		
Reference spacing D of UAF	**Minimum**	**Maximum**	**Average**
3000λ	−5.251	−4.523	−4.879
300λ	−6.064	−4.590	−5.082
30λ	−15.822	−11.865	−14.360
3λ	−31.037	−30.636	−30.821

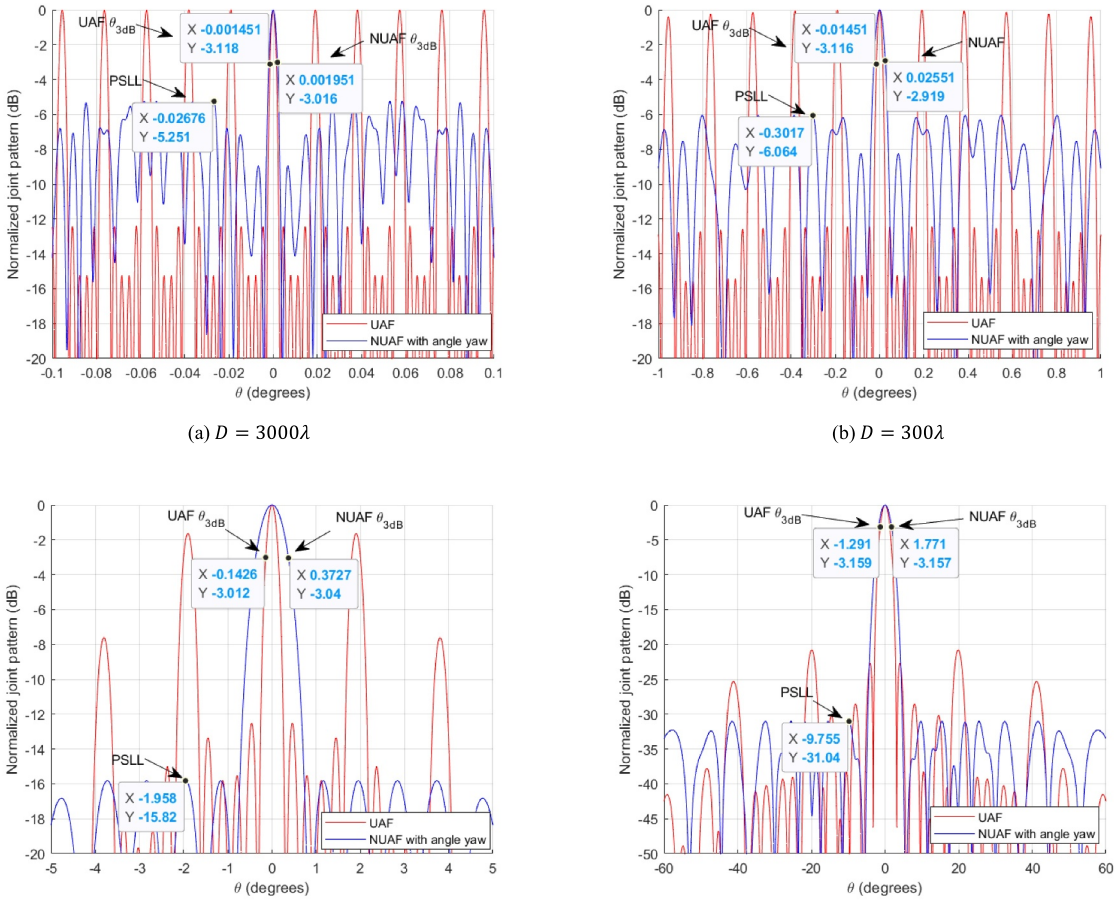

(a) $D = 3000\lambda$ (b) $D = 300\lambda$

(c) $D = 30\lambda$ (d) $D = 3\lambda$

FIGURE 7 | The NUAF joint pattern of PSLL minimum at different reference spacing based on random angle.

PSO still has the best convergence speed and accuracy with better stability.

Based on the side lobe simulation results of NUAF and the UAF random angle yaw mentioned above, it is important to highlight the following:

- PSLL minimum: NUAF random angle yaw > NUAF > UAF random angle yaw.
- Beamwidth: NUAF random angle yaw < NUAF < UAF random angle yaw.
- PSLL minimum convergence speed: NUAF ≈ NUAF random angle yaw < UAF.

Additionally, it should be noted that the minimum of PSLL is only the result under the conditions of 6 RUs and 20 RU antenna elements. If the number of RUs and RU antenna elements increases, the minimum of PSLL will further decrease. It should also be emphasised that the spacings $D = 3\lambda$ and $D = 30\lambda$ primarily serve as theoretical reference values for array antenna design studies. For practical orbital implementation, the larger spacings of $D = 300\lambda$ and $D = 3000\lambda$ are more operationally feasible as they better satisfy both coherent baseline requirements and inter-satellite safety distance constraints.

6 | Conclusions

This article establishes a joint pattern model of DSCAR based on UAF and provides expressions for the joint pattern. In order to effectively suppress the grating lobe generated by UAF, this article proposes three non-periodic geometric formations methods: NUAF, UAF random angle yaw and NUAF random angle yaw. Meanwhile, this article designs a segmented IF PSO to optimize the parameters of non-uniform distribution spacing and random yaw angle, and obtains the PSLL and beamwidth of three non-periodic geometric formations based on four typical reference uniform spacing. When DSCAR has less the number of RU and RU antenna elements, the NUAF random angle yaw has the surprisingly best suppression effect on PSLL but the unexpected relatively widest beamwidth, whereas the UAF random angle yaw suppression has a limited effect but the smallest extent of beamwidth spread. In the meantime, NUAF falls between the two. As the RU spacing decreases, the suppression effect on PSLL improves which has highly referenced

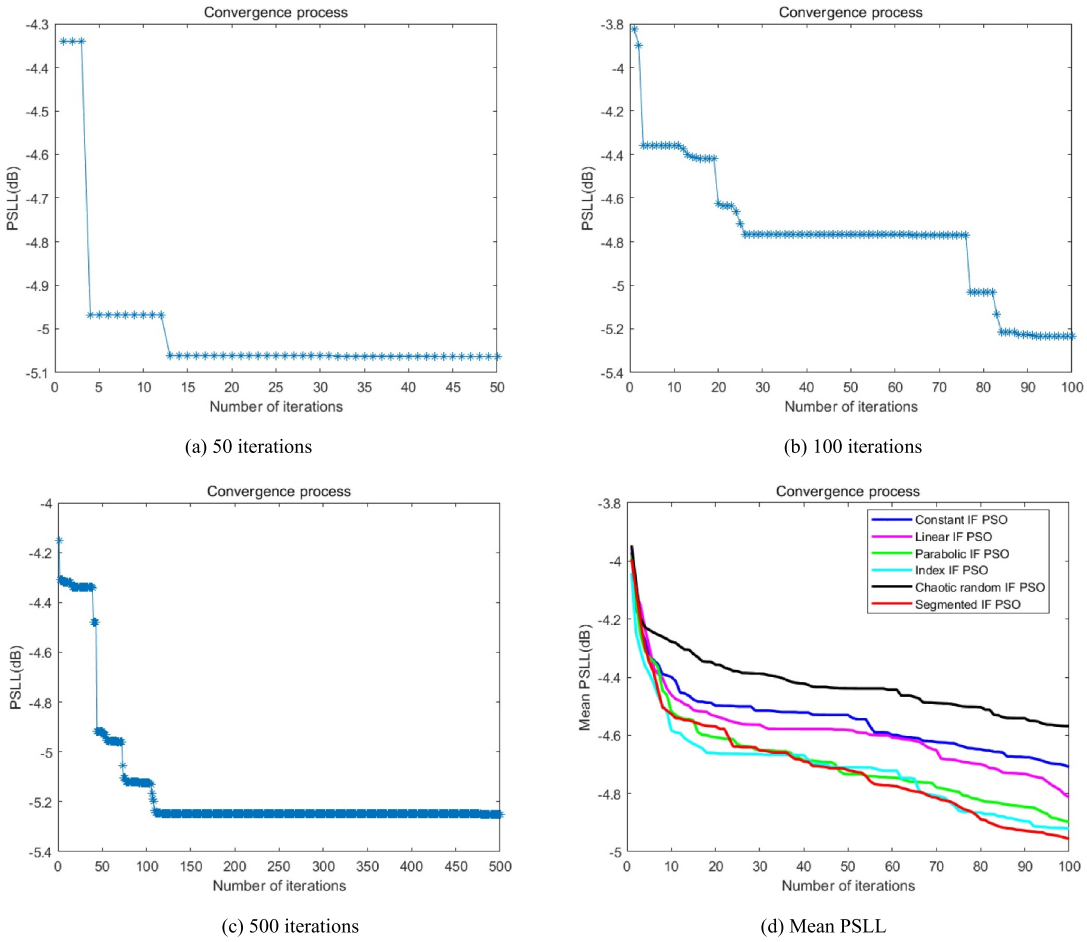

(a) 50 iterations

(b) 100 iterations

(c) 500 iterations

(d) Mean PSLL

FIGURE 8 | PSLL suppression results.

value for low side lobe design in phased array antennas. Furthermore, compared with other IF PSO, we also use benchmark functions to test and verify the performance of the segmented IF PSO multiple times. The verification results showed that segmented IF PSO has significant advantages in convergence speed and optimization accuracy.

Author Contributions

Lin Qiu: conceptualisation, data curation, formal analysis, funding acquisition, investigation, methodology, project administration, resources, software, supervision, validation, visualisation, writing – original draft, writing – review and editing. **Huijie Liu:** formal analysis, resources, supervision, writing – review and editing. **Juan Chen:** investigation, writing – review and editing. **Hao Huang:** funding acquisition, resources. **Andrew W. H. Ip:** funding acquisition, resources, supervision. **Kai Leung Yung:** funding acquisition, resources, supervision.

Acknowledgements

This work is supported in part by the Youth Innovation Promotion Association of the Chinese Academy of Sciences under (Grant No. 2022296), in part by the Hubei Province International Scientific Research Cooperation Project under (Grant No. 2023EHA035) and in part by the Research Centre for Deep Space Explorations of the Hong Kong Polytechnic University (Grant No. K-45-35-ZPEV).

Conflicts of Interest

The authors declare no conflicts of interest.

Data Availability Statement

Data sharing is not applicable to this article as no datasets were generated or analysed during this study.

References

1. Z. Yang, G. Liao, and C. Zeng, "Reduced-Dimensional Processing for Ground Moving Target Detection in Distributed Space-Based Radar," *IEEE Geoscience and Remote Sensing Letters* 4, no. 2 (2007): 256–259, https://doi.org/10.1109/lgrs.2007.890547.

2. P. Huang, G. Liao, Z. Yang, Y. Shu, and W. Du, "Approach for Space-Based Radar Manoeuvring Target Detection and High-Order Motion Parameter Estimation," *IET Radar, Sonar & Navigation* 9, no. 6 (2015): 732–741, https://doi.org/10.1049/iet-rsn.2014.0192.

3. R. Hoffmann, S. Jonkers, R. Kohlleppel, et al., "Performance Evaluation of a Distributed Radar System for Space Surveillance," in *2019 IEEE Radar Conference (RadarConf)* (IEEE, 2019), 1–6.

4. J. Chen, P. Huang, X. G. Xia, et al., "Multichannel Signal Modeling and AMTI Performance Analysis for Distributed Space-Based Radar Systems," *IEEE Transactions on Geoscience and Remote Sensing* 60 (2022): 1–24, https://doi.org/10.1109/tgrs.2022.3202567.

5. H. Steyskal, J. K. Schindler, P. Franchi, and R. Mailloux, "Pattern Synthesis for TechSat21-A Distributed Space-Based Radar System,"

IEEE Antennas and Propagation Magazine 45, no. 4 (2003): 19–25, https://doi.org/10.1109/map.2003.1241307.

6. P. Jin, Z. Li, and J. Wang, "The Array Design of the Distributed Space-Based Radar Based on Sunflower Arrays," in *2016 11th International Symposium on Antennas, Propagation and EM Theory (ISAPE)* (IEEE, 2016), 283–286.

7. W. Wang, Y. Liu, C. Duan, et al., "Discrete Side-Lobe Clutter Suppression by Designing Orthogonal Projection Filter in Space-Based Radar Systems," in *IET International Radar Conference (IET IRC 2020)* (IET, 2020), 892–896.

8. Y. Li, W. Yang, Q. Li, et al., "A Discrete Side-Lobe Clutter Recognition Method Based on Sliding Filter Response Loss for Space-Based Radar," *Frontiers in Physics* 11 (2023): 1142154, https://doi.org/10.3389/fphy.2023.1142154.

9. N. Qiao, S. Zhang, T. Zhang, and Y. Wang, "Clutter Characteristic Analysis and Grating Lobe Suppression for Distributed Small Satellite Space-Based Early Warning Radar," *IEEE Transactions on Aerospace and Electronic Systems* 59, no. 6 (2023): 7977–7992, https://doi.org/10.1109/taes.2023.3298590.

10. A. B. Smolders and H. J. Visser, "Low Side-Lobe Circularly-Polarized Phased Arrays Using a Random Sequential Rotation Technique," *IEEE Transactions on Antennas and Propagation* 62, no. 12 (2014): 6476–6481, https://doi.org/10.1109/tap.2014.2359476.

11. P. Rocca, R. J. Mailloux, and G. Toso, "GA-Based Optimization of Irregular Subarray Layouts for Wideband Phased Arrays Design," *IEEE Antennas and Wireless Propagation Letters* 14 (2014): 131–134, https://doi.org/10.1109/lawp.2014.2356855.

12. N. Anselmi, P. Rocca, M. Salucci, and A. Massa, "Irregular Phased Array Tiling by Means of Analytic Schemata-Driven Optimization," *IEEE Transactions on Antennas and Propagation* 65, no. 9 (2017): 4495–4510, https://doi.org/10.1109/tap.2017.2722539.

13. A. Alshammary, S. Weiss, and S. Almorqi, "Grating Lobe Suppression in Rotationally Tiled Arrays," in *2017 11th European Conference on Antennas and Propagation (EUCAP)* (IEEE, 2017), 1158–1161.

14. J. Yu, V. A. Khlebnikov, and M. H. Ka, "Wideband Grating-Lobe Suppression by Rotation of the Phased Array Stations in the SKA Low-Frequency Sparse Aperture Array," *IEEE Transactions on Antennas and Propagation* 63, no. 9 (2015): 3939–3946, https://doi.org/10.1109/tap.2015.2452965.

15. J. Zhu, P. Lei, J. Wang, Y. Zhang, and C. Yuan, "Grating Lobe Suppression and Angle Estimation Based on Virtual Antennas Filling in Sparse Array," *IEEE Antennas and Wireless Propagation Letters* 22, no. 3 (2022): 502–506, https://doi.org/10.1109/lawp.2022.3216886.

16. X. Xu, C. Liao, L. Zhou, and F. Peng, "Grating Lobe Suppression of Non-Uniform Arrays Based on Position Gradient and Sigmoid Function," *IEEE Access* 7 (2019): 106407–106416, https://doi.org/10.1109/access.2019.2932123.

17. E. Anarakifirooz and S. Loyka, "Structural Design of Non-Uniform Linear Arrays for Favorable Propagation in Massive MIMO," *IEEE Communications Letters* 27, no. 1 (2022): 367–371, https://doi.org/10.1109/lcomm.2022.3210826.

18. G. Yang, H. Zeng, and Z. Xu, "Adaptive Gradient Search Algorithm for Displaced Subarrays With Large Element Spacing," *IEEE Antennas and Wireless Propagation Letters* 20, no. 7 (2021): 1155–1159, https://doi.org/10.1109/lawp.2021.3074253.

19. L. Liang, J. Sun, H. Li, J. Liu, Y. Jiang, and J. Zhou, "Research on Side Lobe Suppression of Time-Modulated Sparse Linear Array Based on Particle Swarm Optimization," *International Journal of Antennas and Propagation* 2019, no. 1 (2019): 7130106–7130114, https://doi.org/10.1155/2019/7130106.

20. Q. Nguyen and G. Mitchell, "A Particle Swarm Approach to Grating Lobe Suppression in an Aperiodic Vivaldi Array," in *2022 United States National Committee of URSI National Radio Science Meeting (USNC-URSI NRSM)* (IEEE, 2022), 264–265.

21. G. Tashtarian and M. S. Majedi, "Grating Lobes Reduction in Linear Arrays Composed of Subarrays Using PSO," in *2019 International Symposium on Networks, Computers and Communications (ISNCC)* (IEEE, 2019), 1–6.

22. I. C. Trelea, "The Particle Swarm Optimization Algorithm: Convergence Analysis and Parameter Selection," *Information Processing Letters* 85, no. 6 (2003): 317–325, https://doi.org/10.1016/s0020-0190(02)00447-7.

23. Y. Shi and R. Eberhart, "A Modified Particle Swarm Optimize," in *1998 IEEE International Conference on Evolutionary Computation Proceedings. IEEE World Congress on Computational Intelligence (Cat. No. 98TH8360)* (IEEE, 1998), 69–73.

24. A. Chatterjee and P. Siarry, "Nonlinear Inertia Weight Variation for Dynamic Adaptation in Particle Swarm Optimization," *Computers & Operations Research* 33, no. 3 (2006): 859–871, https://doi.org/10.1016/j.cor.2004.08.012.

25. J. Chuanwen and E. Bompard, "A Self-Adaptive Chaotic Particle Swarm Algorithm for Short Term Hydroelectric System Scheduling in Deregulated Environment," *Energy Conversion and Management* 46, no. 17 (2005): 2689–2696, https://doi.org/10.1016/j.enconman.2005.01.002.

26. Y. Feng, G. F. Teng, A. X. Wang, et al., "Chaotic Inertia Weight in Particle Swarm Optimization," in *Second International Conference on Innovative Computing, Informatio and Control (ICICIC 2007)* (IEEE, 2007), 475.

27. M. Taherkhani and R. Safabakhsh, "A Novel Stability-Based Adaptive Inertia Weight for Particle Swarm Optimization," *Applied Soft Computing* 38 (2016): 281–295, https://doi.org/10.1016/j.asoc.2015.10.004.

28. K. R. Harrison, A. P. Engelbrecht, and B. M. Ombuki-Berman, "Inertia Weight Control Strategies for Particle Swarm Optimization: Too Much Momentum, Not Enough Analysis," *Swarm Intelligence* 10, no. 4 (2016): 267–305, https://doi.org/10.1007/s11721-016-0128-z.

29. X. Yao, Y. Liu, and G. Lin, "Evolutionary Programming Made Faster," *IEEE Transactions on Evolutionary Computation* 3, no. 2 (1999): 82–102, https://doi.org/10.1109/4235.771163.

Appendix

TABLE A1 | The 23 benchmark functions.

Function no.	Test function	n	S	$f_{\min}$
F1	$f_1(x) = \sum_{i=1}^{n} x_i^2$	30	$[-100, 100]^n$	0
F2	$f_2(x) = \sum_{i=1}^{n} \lvert x_i \rvert + \prod_{i=1}^{n} \lvert x_i \rvert$	30	$[-10, 10]^n$	0
F3	$f_3(x) = \sum_{i=1}^{n} \left(\sum_{j=1}^{i} x_j\right)^2$	30	$[-100, 100]^n$	0
F4	$f_4(x) = \max_i\{\lvert x_i \rvert, 1 \le i \le n\}$	30	$[-100, 100]^n$	0
F5	$f_5(x) = \sum_{i=1}^{n-1} \left[100\left(x_{i+1} - x_i^2\right)^2 + (x_i - 1)^2\right]$	30	$[-30, 30]^n$	0
F6	$f_6(x) = \sum_{i=1}^{n} (\lfloor x_i + 0.5 \rfloor)^2$	30	$[-100, 100]^n$	0
F7	$f_7(x) = \sum_{i=1}^{n} i x_i^4 + \text{random}[0, 1)$	30	$[-1.28, 1.28]^n$	0
F8	$f_8(x) = \sum_{i=1}^{n} -x_i \sin\left(\sqrt{\lvert x_i \rvert}\right)$	30	$[-500, 500]^n$	−12569.5
F9	$f_9(x) = \sum_{i=1}^{n} \left[x_i^2 - 10\cos(2\pi x_i) + 10\right]$	30	$[-5.12, 5.12]^n$	0
F10	$f_{10}(x) = -20\exp\left(-0.2\sqrt{\frac{1}{n}\sum_{i=1}^{n} x_i^2}\right) - \exp\left(\frac{1}{n}\sum_{i=1}^{n} \cos 2\pi x_i\right) + 20 + e$	30	$[-32, 32]^n$	0
F11	$f_{11}(x) = \frac{1}{4000}\sum_{i=1}^{n} x_i^2 - \prod_{i=1}^{n} \cos\left(\frac{x_i}{\sqrt{i}}\right) + 1$	30	$[-600, 600]^n$	0
F12	$f_{12}(x) = \frac{\pi}{n}\left\{10\sin^2(\pi y_i) + \sum_{i=1}^{n-1} (y_i - 1)^2\left[1 + 10\sin^2(\pi y_{i+1})\right] + (y_n - 1)^2\right\}$ $+\sum_{i=1}^{n} u(x_i, 10, 100, 4)$ $y_i = 1 + \frac{1}{4}(x_i + 1)$ $u(x_i, a, k, m) = \begin{cases} k(x_i - a)^m, x_i > a \\ 0, -a \le x_i \le a \\ k(-x_i - a)^m, x_i < -a \end{cases}$	30	$[-50, 50]^n$	0
F13	$f_{13}(x) = 0.1\left\{\sin^2(3\pi x_i) + \sum_{i=1}^{n-1} (x_i - 1)^2\left[1 + \sin^2(3\pi x_{i+1})\right] + (x_n - 1)^2\left[1 + \sin^2(2\pi x_n)\right]\right\} + \sum_{i=1}^{n} u(x_i, 5, 100, 4)$	30	$[-50, 50]^n$	0
F14	$f_{14}(x) = \left[\frac{1}{500} + \sum_{j=1}^{25} \frac{1}{j + \sum_{i=1}^{2} (x_i - a_{ij})^6}\right]^{-1}$	2	$[-65.536, 65.536]^n$	1
F15	$f_{15}(x) = \sum_{i=1}^{11} \left[a_i - \frac{x_i\left(b_i^2 + b_i x_2\right)}{b_i^2 + b_i x_3 + x_4}\right]^2$	4	$[-5, 5]^n$	3.075e-4
F16	$f_{16}(x) = 4x_1^2 - 2.1x_1^4 + \frac{1}{3}x_1^6 + x_1 x_2 - 4x_2^2 + 4x_2^4$	2	$[-5, 5]^n$	−1.0316
F17	$f_{17}(x) = \left(x_2 - \frac{5.1}{4\pi^2}x_1^2 + \frac{5}{\pi}x_1 - 6\right)^2 + 10\left(1 - \frac{1}{8\pi}\right)\cos x_1 + 10$	2	$[-5, 10] \times [0, 15]$	0.398
F18	$f_{18}(x) = \left[1 + (x_1 + x_2 + 1)^2\left(19 - 14x_1 + 3x_1^2 - 14x_2 + 6x_1 x_2 + 3x_2^2\right)\right] \times \left[30 + (2x_1 - 3x_2)^2\left(18 - 32x_1 + 12x_1^2 + 48x_2 - 36x_1 x_2 + 27x_2^2\right)\right]$	2	$[-2, 2]^n$	3
F19	$f_{19}(x) = -\sum_{i=1}^{4} c_i \exp\left[-\sum_{j=1}^{4} a_{i,j}\left(x_j - p_{i,j}\right)^2\right]$	4	$[0, 1]^n$	−3.86
F20	$f_{20}(x) = -\sum_{i=1}^{4} c_i \exp\left[-\sum_{j=1}^{6} a_{i,j}\left(x_j - p_{i,j}\right)^2\right]$	6	$[0, 1]^n$	−3.32
F21	$f_{21}(x) = -\sum_{i=1}^{5} \left[(x - a_i)(x - a_i)^T + c_i\right]^{-1}$	4	$[0, 10]^n$	−10
F22	$f_{22}(x) = -\sum_{i=1}^{5} \left[(x - a_i)(x - a_i)^T + c_i\right]^{-1}$	4	$[0, 10]^n$	−10
F23	$f_{23}(x) = -\sum_{i=1}^{5} \left[(x - a_i)(x - a_i)^T + c_i\right]^{-1}$	4	$[0, 10]^n$	−10